

Hamiltonian Dynamics of Yang-Mills Fields on a Lattice

T.S. Biró

Institut für Theoretische Physik, Justus-Liebig-Universität, D-6300 Giessen, Germany

C. Gong and B. Müller

Department of Physics, Duke University, Durham, NC 27708

A. Trayanov

NCSC, Research Triangle Park, NC 27709

(Dated: July 2, 2018)

Abstract

We review recent results from studies of the dynamics of classical Yang-Mills fields on a lattice. We discuss the numerical techniques employed in solving the classical lattice Yang-Mills equations in real time, and present results exhibiting the universal chaotic behavior of nonabelian gauge theories. The complete spectrum of Lyapunov exponents is determined for the gauge group $SU(2)$. We survey results obtained for the $SU(3)$ gauge theory and other nonlinear field theories. We also discuss the relevance of these results to the problem of thermalization in gauge theories.

I. INTRODUCTION

Knowledge of the microscopic mechanisms responsible for the local equilibration of energy and momentum carried by nonabelian gauge fields is important for our understanding of non-equilibrium processes occurring in the very early universe and in relativistic nuclear collisions. Prime examples for such processes are baryogenesis during the electroweak phase transition, the creation of primordial fluctuations in the density of galaxies in cosmology, and the formation of a quark-gluon plasma in heavy-ion collisions.

Whereas transport and equilibration processes have been extensively investigated in the framework of perturbative quantum field theory, rigorous non-perturbative studies of non-abelian gauge theories have been limited to systems at thermal equilibrium. We here review recent numerical studies of real-time evolution in the classical limit of lattice gauge theories. We will demonstrate that such an analysis can provide valuable insight into the dynamical properties of nonabelian gauge theories at high excitation energies.

This paper is organized as follows. In section 2, we briefly discuss why a classical consideration of gauge fields is relevant, and we review the early studies of evidence for chaotic behavior of Yang-Mills fields. Section 3 is devoted to the results of our lattice study on SU(2) gauge theory. After some general considerations, we introduce the lattice formalism of gauge fields, and we describe the numerical techniques used to solve the field equations. Then we show the exponential divergence of two nearby trajectories, from which we can conclude that the system is chaotic, and extract the maximal Lyapunov exponent. In the last two subsections of section 3, we show how one can obtain the whole Lyapunov spectrum. After the experience with SU(2), results of several other theories are reviewed in section 4. These include compact U(1) and SU(3) gauge theory, massless Higgs fields, massive SU(2) vector fields, and finally the coupled SU(2) gauge-Higgs system. In section 5, we discuss one application of chaoticity in nonabelian gauge theory, namely, the thermalization process of highly excited gauge fields. We estimate the time needed to thermalize the system from the Kolmogorov-Sinai entropy of the gauge field. This time agrees with the results from thermal perturbation theory, supporting the view that the thermalization of the long wavelength modes is basically a classical process. Finally, in section 6, we point out some possible avenues of future work in this field, both in regard to the method itself and to physical applications.

II. GAUGE FIELDS IN THE CLASSICAL LIMIT

A. General Considerations

Let us start by discussing the classical limit of a simple system with a single degree of freedom which is described by a Hamiltonian

$$H(p, x) = \frac{1}{2}p^2 + V(x), \quad (1)$$

where $V(x)$ is some well defined potential. The quantum evolution is defined either by operator equations for p and x in Heisenberg picture,

$$\begin{aligned} \dot{x} &= p, \\ \dot{p} &= -\partial_x V(x), \end{aligned} \quad (2)$$

or by a Schrödinger equation for the wave function,

$$i\hbar\partial_t\Phi = \hat{H}\Phi. \quad (3)$$

Both are appropriate to describe the behavior of a pure state. To admit mixed states it is necessary to use the quantum Liouville equation

$$i\hbar\partial_t\rho = [H, \rho] \quad (4)$$

for the density matrix ρ . For a system in a pure state, $\rho = |\Phi\rangle\langle\Phi|$, the Liouville equation is reduced to the Schrödinger equation.

Quantum mechanics and classical mechanics are related by the correspondence principle, which states that at large quantum numbers or small \hbar quantum mechanics has classical mechanics as a limit. But it is not trivial to actually construct the correspondence, especially when the system considered is chaotic in the classical limit. Quantum chaos is still far from being a well understood concept [2].

In the Heisenberg picture the classical limit is attained by treating the operator equations as equations of real numbers, i.e. by neglecting the non-commutivity of x and p which is of the order of \hbar . The classical limit is equivalent to the limit $\hbar \rightarrow 0$. The advantage of working in this picture is that the classical limit is directly reached by the above simple prescription. The disadvantage is that it is difficult to estimate the accuracy of the classical approach.

In the Schrödinger picture, it is useful to consider wave functions which have minimum spread in both momentum and space representation. When the system is highly excited, i.e. the accessible phase space is much larger than the volume of the wave packet, it describes a state for which both x and p have “sharp” values. The classical equations of x and p are

obtained by calculating time derivatives of expectation values of x and p under such a wave function evolving according to the Schrödinger equation and neglecting the corrections due to the finite width of the wave packet. These corrections can be shown to be of the order of \hbar and hence can be neglected for a highly excited system. The problem in this representation is that as the system evolves with time, the minimum uncertainty may not be maintained due to the influence of interactions. The width of the wave packet may start to increase and the classical equations may become invalid. This problem is especially serious for classically chaotic systems. An exact quantum calculation has been done for the “Arnold Cat” system which is chaotic in the classical limit. It was shown that an initially sharp Gaussian wave packet quickly dissolves into a diffuse state which is anything but a Gaussian [3]. Hence we must be especially cautious when we talk about a localized wave packet in a chaotic quantum system.

Another way to compare classical and quantum mechanics is to work with the Wigner function $W(p, x)$ which is defined as

$$W(p, x) = \int_{-\infty}^{+\infty} dy e^{-ipy/\hbar} \langle x + \frac{1}{2}y | \rho | x - \frac{1}{2}y \rangle. \quad (5)$$

From the Liouville equation we can derive the time evolution of $W(p, x)$,

$$\frac{\partial W}{\partial t} = (\mathcal{L}_c + \mathcal{L}_q)W \quad (6)$$

where \mathcal{L}_c is the classical Liouville operator which describes the classical dynamics in phase space language,

$$\mathcal{L}_c = (\partial_p H) \partial_x - (\partial_x H) \partial_p, \quad (7)$$

while \mathcal{L}_q comprises the quantum corrections

$$\mathcal{L}_q = \frac{\hbar^2}{24} (\partial_x^3 V) \partial_p^3 - \frac{\hbar^4}{1920} (\partial_x^5 V) \partial_p^5 + \dots \quad (8)$$

which are of successively higher order in \hbar . In principle, in this representation the quantum corrections to the classical calculation can be computed order by order in \hbar . The rapid dissolution of localized wave packets for chaotic systems has also been observed in the Wigner representation [4], and some attempts have been made to include quantum corrections by means of a stochastic process [5]. The Wigner function approach has been invoked to derive transport equations for gauge theories in the mean-field approximation [6], but to our knowledge it has not yet been applied to gauge theories on a lattice.

B. Classical Limit of a Gauge Theory

Now let us turn our attention to nonabelian gauge fields, where we are dealing with a system of infinitely many degrees of freedom. What does it mean in this case that the system is highly excited? Certainly not every degree of freedom can be highly excited, because this would require an infinite amount of energy. To this end it is better to look at the system in Fock space. The system is excited by creating particles with different energy E and momentum $\hbar k$. Now suppose the gauge field is excited to a temperature T . The Bose distribution function implies that the long wavelength particles are more copiously excited. For $E \ll T$ the Bose distribution $(e^{E/T} - 1)^{-1}$ merges into classical distribution function T/E , whereas the “hard” particles of short wavelength are rarely excited. So, generally, the long wavelength modes can be treated classically and the short wavelength modes retain their quantum statistics. With increasing T , or decreasing \hbar , more and more modes approach the classical limit. If, at certain temperature, a physical quantity is only related to long wavelength modes, then we expect the classical calculation to be adequate and the quantum corrections to be small.

It is here where the lattice regularization of the gauge field plays an essential role. While being originally advocated [7] as gauge-invariant cut-off of the ultraviolet divergencies of the quantum field theory, it can assume a new role in the definition of the classical high-temperature limit of the quantum field theory. In the lattice formulation all modes with wavelength shorter than the lattice spacing a are eliminated, and we are left only with the infrared modes. Hence the lattice regulated gauge theory generally goes to the classical limit at high temperature $T \gg \hbar/a$ or vanishing \hbar . The validity of the classical calculation may depend on the nature of the quantity we are interested in. For example we will show later that the damping rate for a gluon at rest, as well as the rate of thermalization, are essentially classical quantities, because they are induced by the interaction of long wavelength modes. On the other hand, the screening length of static electric gauge fields is controlled by short wavelength modes, and hence is at best a semi-classical quantity.

The second problem is how to derive the classical field equation from the quantum field equation. Does the classical equation make any sense? This question is related to the confinement problem. We can see this as follows. In the Heisenberg picture we can start with the operator equation

$$D_\mu F^{\mu\nu} = 0, \tag{9}$$

where D is the covariant derivative and F is the field operator. The classical equation is obtained by treating F and A as numbers rather than operators. We call $F(x)$ and $A(x)$ classical field configurations. Suppose now we want to work in the Schrödinger picture. In

an unbroken nonabelian gauge theory, for example in QCD, we observe color confinement so that only color singlet states are physically realizable. If we calculate the expectation value of a (color-octet) electric field component $E^a(x)$ in a singlet state, the result vanishes according to the Wigner-Eckart theorem. This means that a classical configuration does not correspond trivially to a physical state with minimum uncertainty. The reason is that a classical gauge configuration is only gauge covariant while a singlet state is gauge invariant. But this does not mean that there is no relation between them. We can start from a classical configuration and gauge rotate it to obtain other configurations. We then superimpose these to form a singlet state which corresponds to a physical state. This procedure corresponds to the Peierls-Yoccoz projection method [8] for wavefunctions with good symmetry properties. We can reverse the process and decompose a highly excited color singlet state into some “nearly classical” configurations. By studying these configurations classically, we can gain insight into the evolution of the original physical state.

C. Reasons for Investigating the Classical Limit

The most commonly used approximation method in quantum field theory is perturbation theory. But we know that in nonabelian gauge theory there exist some fundamental non-perturbative effects, such as color confinement and topological quantum numbers. These effects are beyond the reach of perturbation theory; non-perturbative methods are required to understand them. The investigation of gauge fields in the classical limit provides one such approach. Studies of the classical field equations have led to some very interesting non-perturbative results, such as monopole solutions and instantons [9, 10]. These classical solutions prove to be vital to the understanding of the corresponding quantum physics. On the other hand, these solutions are not general integrals of the classical non-linear gauge field equations, but exploit special symmetries of the nonabelian gauge theory. In any case, the known classical solutions of the Yang-Mills equations are by no means exhaustive, and the equations have been shown to be nonintegrable in general [11]. Thus we do not have a complete understanding even for the classical field equations. It is our hope to learn something about the general behavior of nonabelian gauge fields by numerically integrating the classical equations of motion.

Secondly, under some extreme conditions, e.g. at high temperature, the quantum field reaches its classical limit at least for some observables. Quantities that are calculable in the classical limit can be identified in the high-temperature expansion of perturbation theory as those that exhibit a leading term proportional to g^2T . Namely, if g is the coupling constant of the classical gauge theory, related to the standard dimensionless gauge coupling constant $\alpha = g^2\hbar/4\pi$, the term g^2T has the dimension of an inverse length or time and survives in

the limit $\hbar \rightarrow 0$. Quantities with this leading behavior are, e.g., the gluon damping rate [12] and perhaps the inverse screening length of static magnetic gauge fields [13, 14]. If we are interested in these quantities, the classical approach can provide us with a practical method of calculating these physical observables.

D. Chaotic Dynamics of Yang-Mills Fields

The first evidence that Yang-Mills fields exhibit chaotic dynamics was found a decade ago by Matinyan, Savvidy, and others [11, 15, 16, 17], when they studied the dynamics of spatially constant potentials in the SU(2) gauge theory. In contrast to electrodynamics, such potentials are not always gauge equivalent to the trivial vacuum, due to the non-commutative nature of gauge transformations in nonabelian gauge theories. The original motivation for these studies was the desire to show that the Yang-Mills equations form a non-integrable dynamical system; it obviously suffices to prove this assertion in a limiting case. However one can also regard constant potentials as the relevant degrees of freedom surviving in the infrared limit. Indeed, Lüscher has shown that the Hamiltonian (1) appears as lowest order term in the effective action for the Yang-Mills theory on a three-dimensional torus, i.e. in a cubic box with periodic boundary conditions [19].

Choosing the temporal gauge $A_0^a = 0$ ($a = 1, 2, 3$), and assuming that the vector potentials $\mathbf{A}^a(t)$ are functions of time only, the dynamics is governed by the Hamiltonian

$$H_{\text{YM}} = \sum_a \frac{1}{2}(\dot{\mathbf{A}}^a)^2 + \frac{1}{4}g^2 \sum_{a,b} (\mathbf{A}^a \times \mathbf{A}^b)^2, \quad (10)$$

where g is the gauge coupling constant. It is not hard to show that the system allows for seven integrals of motion, corresponding to energy, angular momentum, and color charge conservation. In fact, the Hamiltonian can be reduced to the form

$$H_{\text{YM}} \simeq \frac{1}{2}(\dot{x}^2 + \dot{y}^2 + \dot{z}^2) + \frac{1}{2}g^2(x^2y^2 + y^2z^2 + z^2x^2) + \dots \quad (11)$$

where the dots indicate terms describing quasi-rotational degrees of freedom. The nontrivial dynamical aspects are all contained in the three variables $x(t)$, $y(t)$, $z(t)$. Note that the coupling constant g can be eliminated by rescaling the time coordinate. It is therefore useful to introduce an additional term into the Hamiltonian which breaks this scale invariance, e.g., a harmonic potential:

$$H_{\text{YMH}} = H_{\text{YM}} + \frac{1}{4}g^2v^2(x^2 + y^2 + z^2). \quad (12)$$

The dynamical properties of this Hamiltonian are controlled by the dimensionless parameter

$$r = \frac{1}{4}(gv)^4/g^2E, \quad (13)$$

where E is the energy density. Numerical studies of Poincaré surfaces of section of trajectories revealed [11] that the motion governed by the Hamiltonian (12) is regular for values $r \gg 1$, becoming partially chaotic as r falls below 1, and strongly chaotic for $r \rightarrow 0$, as shown in Figure 1. The mechanism leading to divergence of nearby trajectories is similar to a classical billiard: the equipotential boundary of classical motion for a given energy E has negative curvature. A singular-point analysis of the system (12) has been performed by Steeb et al. [20]. It is not known whether the Hamiltonian (11) describes a true K-system, this conjecture has been refuted for the two-dimensional analogue [21]

Space-dependent solutions of the Yang-Mills equation have been studied in the case of spherical symmetry for solutions of the form [22, 23, 24]

$$A_i^a = -\varepsilon_{aik} \frac{x_k}{r^2} (1 + \phi(r, t)), \quad (14)$$

which include the so-called Wu-Yang monopole ($\phi \equiv 0$). The radial function $\phi(r, t)$ satisfies the nonlinear wave equation

$$(\partial_t^2 - \partial_r^2)\phi = \frac{1}{r^2}\phi(1 - \phi^2), \quad (15)$$

which has been shown to exhibit the rapid energy sharing between Fourier components which is characteristic of chaotic systems [22, 23]. Equation (15) has also been shown to be non-integrable by the method of Painlevé analysis [24].

Recently, solutions of the Yang-Mills equations in two spatial dimensions have been studied numerically, subject to the assumption that the potentials A_i^a depend only on one spatial coordinate and on time [25]. Again mode-sharing of the energy was observed, and there are indications that the spatial potential functions evolve into a fractal pattern.

III. CHAOS IN SU(2) LATTICE GAUGE THEORY

A. General Considerations

Interesting as these results are, they leave two important questions unanswered: What are the dynamical properties of the full (3+1)-dimensional classical Yang-Mills field? What is the physical significance of chaotic dynamics of the classical field theory? The goal of our investigation was to provide at least partial answers to these questions. Our approach [26] deviates in two important aspects from earlier studies:

(a) Since the spatial coordinates have to be discretized for numerical purposes, it is convenient to formulate the SU(2)-gauge theory in terms of matrix-valued link variables on a N^3 cubic lattice [7, 27]:

$$U_{x,i} = \exp\left(-\frac{1}{2}igaA_i^a(x)\tau^a\right). \quad (16)$$

Here τ^a are the Pauli matrices, a is the elementary lattice spacing, and (x, i) denotes the link from the lattice site x to the nearest neighbor in direction i , $x + i$. The link variables $U_{x,i}$ are explicitly gauge covariant, as opposed to the Yang-Mills potentials $A_i^a(x)$. Since the $U_{x,i}$ take values on the gauge group $SU(2)$ rather than the group algebra, the magnetic field strength is bounded for a given lattice spacing.

(b) Instead of studying the gauge field dynamics in the vicinity of arbitrarily selected configurations, we have investigated the dynamical behavior of *random* field configurations, corresponding to gauge fields selected from a microcanonical or canonical ensemble. This has the advantage that our field configurations are controlled by a single parameter, the temperature T or the average energy density ε , which can be varied systematically. This approach also allows for the identification of some quantities calculated for the classical Yang-Mills theory with those obtained in the high-temperature limit of the quantum field theory.

B. Lattice $SU(2)$ Theory in Hamiltonian Formalism

Our study is based on the Hamiltonian formulation of lattice $SU(2)$ -gauge theory [28, 29], governed by the Hamiltonian

$$H = \frac{a}{g^2} \sum_{x,i} \text{tr} (\dot{U}_{x,i}^\dagger \dot{U}_{x,i}) + \frac{4}{g^2 a} \sum_{x,ij} [1 - \frac{1}{2} \text{tr} U_{x,ij}], \quad (17)$$

where a dot denotes the time derivative. Here the electric and magnetic fields have been expressed in terms of the $SU(2)$ link variables $U_{x,i}(t)$ and the so-called plaquette operator $U_{x,ij}$ which is the product of all four link variables on an elementary plaquette with corners $(x, x + i, x + i + j, x + j)$:

$$U_{x,ij} = U_{x,i} U_{x+i,j} U_{x+i+j,-i} U_{x+j,-j} \quad (18)$$

with $U_{x,-i} = U_{x-i,i}^\dagger$. The links are directed and hence the plaquettes are oriented. In the continuum limit the plaquette variable $U_{x,ij}$ is related to the local magnetic field $B_{x,k}^a$

$$U_{x,ij} = \exp(-i \frac{1}{2} g a^2 \epsilon_{ijk} B_{x,k}^a \tau^a), \quad (19)$$

while the electric field on the lattice is given by

$$E_{x,i}^a = -\frac{ia}{g^2} \text{tr} (\tau^a \dot{U}_{x,i} U_{x,i}^\dagger). \quad (20)$$

In the classical limit, this Hamiltonian is scale invariant. To see this explicitly, we scale the time variable, $s = t/a$, obtaining

$$g^2 H a = \sum_{x,i} \text{tr} \left(\frac{\delta U_{x,i}}{\delta s} \frac{\delta U_{x,i}^\dagger}{\delta s} \right) + 4 \sum_{x,ij} [1 - \frac{1}{2} \text{tr} U_{x,ij}], \quad (21)$$

where the right-hand side is parameter free. So the only parameter in the system is total energy or temperature.

The classical equations of motion are derived from this Hamiltonian, making use of the lattice representation of the electric field components (20). It is useful to write the SU(2) matrices in the form

$$U = u_0 - i\tau_a u_a = \begin{pmatrix} u_0 - iu_3 & u_2 - iu_1 \\ -u_2 - iu_1 & u_0 + iu_3 \end{pmatrix} \quad (22)$$

where the u_i are four real numbers, which can be thought of as components of a quaternion. The unit determinant implies that

$$\det U = u_0^2 + u_1^2 + u_2^2 + u_3^2 = 1. \quad (23)$$

One easily verifies that the components of the quaternion satisfy the following differential equations of motion:

$$(\dot{u}_0)_{x,i} = \frac{g^2}{2a} E_{x,i}^a u_{x,i}^a \quad (24)$$

and

$$(\dot{u}_a)_{x,i} = \frac{g^2}{2a} \left[E_{x,i}^a (u_0)_{x,i} + \epsilon^{abc} E_{x,i}^b u_{x,i}^c \right]. \quad (25)$$

These conserve the quaternion length, $\|U\| = \det U$, because they satisfy

$$\dot{u}_0 u_0 + \dot{u}_a u_a = 0. \quad (26)$$

Although it would be sufficient to update only the three fields u_a during the time evolution because of the unit length constraint, it is computationally more efficient to also update the fourth component u_0 , as well using eq. (24) rather than calculating u_0 by taking the square root of $(1 - u_a u_a)$. The three electric fields $E_{x,i}^a$ on each link are updated according to

$$\dot{E}_{x,i}^a = \frac{i}{ag^2} \sum_j \text{tr} \left[\frac{1}{2} \tau^a (U_{x,ij} - U_{x,ij}^\dagger) \right] \quad (27)$$

where the sum runs over all four plaquettes that are attached to the link (x, i) . Here $\text{tr}(\frac{1}{2} \tau^a Q)$, for any quaternion Q , just reads off the component q^a , and therefore does not require additional computational effort.

We note here that the time evolution for the electric field conserves Gauss' law

$$D_i^{ab} E_{x,i}^b = 0, \quad (28)$$

which is an expression of charge conservation. Starting with any configuration $(U_{x,i}, E_{x,i})$ that satisfies Gauss' law, the time evolution will not violate it. Precisely because of the chaotic nature of Yang-Mills dynamics it is, in general, impossible to integrate this set of equations analytically. We have to rely on numerical methods, which will be discussed in the following subsection.

C. Integrating the Equations of Motion

1. Lattice Geometry and Boundary Conditions

In all our simulations we discretize the gauge fields on a simple cubic N^3 lattice with periodic boundary conditions. To calculate the oriented plaquette products more efficiently we use a linked-list approach. All the sites are numbered consecutively. The link numbers are in x , y and z order, and are arranged according to the site of origin. The plaquette numbers are chosen so that they are orthogonal to the links in x , y and z directions, respectively. We also build two additional arrays of numbers at the start of the simulation. One contains the link number of all the links that form a given plaquette, ordered in the way they appear in the directed plaquette product. The other list contains the number of plaquettes that contain a given link, ordered according to the position of the link in the plaquette. The periodic boundary conditions are reflected automatically in the above two link lists.

2. $SU(2)$ Representation

There are several ways to represent a $SU(2)$ matrix: by a complex 2×2 matrix, by a real quaternion, or in polar coordinates as a point on the 4-dimensional unit sphere which can be specified by 3 angles. The last representation has the lowest storage requirements, however, it involves time-consuming trigonometric conversions.

In our simulations we chose the quaternion representation because it takes the least number of floating point operations to multiply two group elements. In the complex matrix representation one needs 32 multiplications and 24 additions compared to 16 floating point multiplications and 12 additions when taking the product of two quaternions. Moreover, the equations of motion can be written in a simpler form in quaternion representation.

3. Numerical Integration

The numerical task consists in propagating the gauge fields in time, by integrating the equations of motion. This can be achieved by a variety of numerical methods. Here we use the Runge-Kutta method with fourth-order accuracy, which is easy to implement, allows for adjustable time-step control, and is quite stable.

The most CPU intense part of the simulation is the computation of the oriented product of the fields over the complement lattice. This complement lattice is defined by all oriented links contained in the elementary plaquette attached to a given link. The overall performance

of the code depends on several issues like field representation, fast access to the data on the neighboring links and plaquettes, etc.

4. *Code Verification and Accuracy*

Several integrals of motion can be used to verify the simulation code and to test the accuracy of the time integration. Since we are studying the Hamiltonian evolution of the gauge fields, the total energy of the system remains constant. With a typical value for the time step of the order of 0.01 dimensionless units, the total energy is conserved to better than 8 significant digits.

Another conserved quantity is the length of each quaternion link variable for SU(2). For an interval less than one dimensionless time unit the conservation is better than 12 significant figures. However, due mainly to accumulation of cut-off and rounding errors the precision is deteriorating progressively. Therefore we choose to rescale the gauge fields after every time integration to maintain fixed length of each dynamical variable, since the subsequent integrations are very sensitive to the quaternion length preservation. This method permits to integrate the equations of motion with a larger time step. Later we will also study SU(3) gauge theory, where the corresponding criterion is that the determinant of the unitary matrix on each link shall be unit. In this respect, the SU(3) evolution is more stable. The deviation of the determinant from one is of order 10^{-8} even if the system evolves over a total time interval of $T = 20$ or 30 .

The validity of Gauss' law, eq. (28), is also an indication for accurate integration, which is extremely sensitive to all kinds of program errors and thus provides a valuable probe for code verification. In our calculations the color charge was always conserved to better than five significant digits.

5. *Performance*

The most time consuming part of the code is the calculation of oriented plaquette products. However, this part of the code is fully vectorizable and runs at about 160 Mflops for SU(2) and 100 Mflops for SU(3) on a single Cray-Y-MP processor. Typically a single time-step integration of the set of equations of motion for $N = 10$ takes about 30 ms CPU time for SU(2) and 220 ms for SU(3) on the same processor.

D. Divergence of Trajectories

In order to look for chaotic motion we will consider the evolution of infinitesimally separated gauge field configurations. If we find exponentially diverging trajectories, we can identify the positive Lyapunov exponents and obtain the value of the Kolmogorov-Sinai entropy, i.e. the entropy growth rate, of the gauge field. To observe the exponential divergence of two trajectories $U_{x,i}(t)$ and $U'_{x,i}(t)$ in the space of gauge field configurations we introduce the following gauge-invariant distance:

$$D[U_{x,i}, U'_{x,i}] = \frac{1}{2N_p} \sum_{x,ij} |\text{tr} U_{x,ij} - \text{tr} U'_{x,ij}|, \quad (29)$$

where $N_p = 3N^3$ is the total number of elementary plaquettes. In the continuum limit

$$D[U_{x,i}, U'_{x,i}] \xrightarrow{a \rightarrow 0} D[A_i^a, A_i^a] \propto \frac{1}{2V} \int d^3x |B'(x)^2 - B(x)^2|, \quad (30)$$

i.e. D measures the average absolute local difference in the magnetic energy of two different gauge fields. We note a peculiar property of this distance measure, which is a natural consequence of the topology of the compact $9N^3$ -dimensional space of magnetic gauge field configurations on the lattice: For $N \gg 1$ almost all pairs of configurations have the same distance D . This is illustrated in Figure 2, where the distribution of distances of randomly chosen configurations from a fixed field configuration is shown for lattices of different size. For large lattices the distribution approaches a narrow Gaussian with a width of order $N^{3/2}$. This property does not limit the usefulness of the metric (29) as measure of the divergence of infinitesimally separate field configurations, but it causes the saturation of D at large times observed in the calculations (see figures below).

Figure 3 shows the evolution of $D(t)$ for initially neighboring gauge field configurations on a 20^3 lattice. We choose the reference configuration by randomly selecting link variables in such a way that the average energy per plaquette takes on the desired value [26]. This procedure is controlled by a parameter δ which varies between 0 and 1. The energy per plaquette grows like δ^2 for small δ and saturates in the limit $\delta \rightarrow 1$. We then construct a neighboring configuration by perturbing each link element infinitesimally (see [26] for details). For values of δ of order unity the distance $D(t)$ starts to grow exponentially as $D(t) = D_0 \exp(ht)$ almost immediately (see Figure 3a). The growth rate h decreases with δ , and for $\delta \ll 1$ one observes an extended period during which the distance $D(t)$ between two adjacent field configurations performs more or less regular oscillations before exponential growth finally sets in (see Figures 3b, 4). For very small values of δ , corresponding to very low energy density of the gauge field configurations, the exponential growth pattern of $D(t)$ is modulated by low-frequency oscillations, which we attribute to the growing influence of non-leading Lyapunov exponents.

The initial latency period before the onset of exponential growth of D can be estimated as follows: We can write $U'_{x,i}(t) = U_{x,i}(t) + \delta U_{x,i}(t)$ where $\delta U_{x,i}$ approximately satisfies a system of linear differential equations with $18N^3$ eigenmodes and eigenfrequencies. On average every eigenmode will be excited with equal probability by our random choice of $\delta U_{x,i}(0)$. In order for the maximally unstable mode to outgrow the combined weight of all other modes we therefore have to wait a certain time t_0 , statistically given by $\exp(ht_0) \approx (18N^3)^{\frac{1}{2}}$, i.e.

$$t_0 \approx \ln(18N^3)/2h. \quad (31)$$

This agrees roughly with the observations, in particular, it explains why the onset of exponential growth is delayed for small values of the slope parameter h (see Figure 4).

E. Maximal Lyapunov Exponents

It is natural to identify the growth rate h with the maximal Lyapunov exponent λ_0 of the lattice gauge theory. This is confirmed by a careful analysis of the Lyapunov spectrum (see sections 3.6 and 3.7 below), and we will assume the equality $h = \lambda_0$ in the following. Extensive studies have shown that λ_0 is a universal function of the average energy per plaquette E , as shown in Figure 5. For values $\delta > 0.15$, the numerical determination of $\lambda_0(E)$ from $D(t)$ is quite reliable, and the statistical and systematic errors are small. Figure 5 demonstrates that $\lambda_0(E)$ is growing approximately linearly with energy. Using the property of scale invariance of the Hamiltonian, discussed previously in eq. (21), one finds that the dimensionless product $\lambda_0 a$ can only be a function of the combination $g^2 E a$. Our numerical results show that this function is approximately linear:

$$\lambda_0 a \approx \frac{1}{6} g^2 E a. \quad (32)$$

This scaling property has been verified numerically over a wide range of values for g and a (see Figure 5). We note that, according to (32), λ_0 is independent of the lattice spacing a in the classical limit, where g does not depend on a .

We have also studied the dependence of $\lambda_0(E)$ on the size of the lattice at fixed lattice spacing a . Figure 7 shows the evolution of the distance between adjacent field configurations for lattices of size ranging from $N = 6$ to $N = 28$. The rapid convergence is obvious, the curves for $N = 28$ hardly deviate from those for $N = 6$, except for a decrease of fluctuations which is not visible in the figure because the curves almost coincide. We have not observed within statistical errors a systematic dependence of $\lambda_0(E)$ on N , for $N \geq 6$ and $\delta > 0.15$. The results obtained for $N = 6$ are shown in Figure 5 as solid squares. For smaller values of δ we found that the exponential growth rate gradually decreases with growing N , which may explain why the lowest two points in Figure 5, obtained for $N = 20$, still lie above the straight line.

F. Rescaling Method for Lyapunov Analysis

The previous method for obtaining the largest Lyapunov exponent of a Hamiltonian system is straightforward, but it has two drawbacks. First, the exponential divergence of trajectories shows fluctuations, resulting in an uncertainty in the determination of the exponential divergence rate. The second drawback of the method is that only the largest Lyapunov exponent can be obtained in this way, but not the complete Lyapunov spectrum. We now discuss a method which can be used to determine Lyapunov exponents more precisely and yields the whole spectrum of Lyapunov exponents.

This technique, which we call rescaling method here, is widely used in studying chaotic dynamical systems [34]. Suppose we want to calculate the two largest Lyapunov exponents of the system. We can randomly choose three initial points in phase space, to which we refer as $z_0(0), z_1(0), z_2(0)$ for convenience, with the condition that they are close to each other according to some appropriate distance measure. If the system is chaotic, or if the initial points are chosen inside the chaotic part of the phase space, the distances between the three trajectories $z_i(t)$ evolved from the three initial points will diverge exponentially. Let us denote the separation vectors between the trajectories by

$$d_i(t) = z_i(t) - z_0(t), \quad (i = 1, 2) \quad (33)$$

and the absolute distance between z_i and z_0 by $D_i = |d_i|$. Since the available phase space volume is limited by the total available energy, $D_i(t)$ will saturate after a certain time. To avoid saturation, the following rescaling method is used. The fixed reference distance $D_0 = D_i(0)$ is chosen in the beginning. The whole procedure consists of two steps. In the first step, the trajectories $z_i(t)$ evolve according to the equations of motion for a period of time t_0 . Then in the second step we rescale the separation vectors d_1 and d_2 as follows. We hold the point $z_0(t_0)$ fixed, but scale the distance D_1 back to D_0 by setting:

$$z'_1(t_0) = z_0(t_0) + \frac{D_0}{D_1(t_0)} d_1(t_0). \quad (34)$$

The scaling factor is denoted by

$$s_1^k = D_1(t_0)/D_0, \quad (35)$$

where k refers to the k th rescaling. For $z_2(t_0)$, we first orthogonalize $d_2(t_0)$ against $d_1(t_0)$, then scale the orthogonalized vector d'_2 to the reference length D_0 . The new scaling factor is denoted by s_2^k . This procedure is iterated n times until the Lyapunov exponents,

$$\lambda_i = \lim_{n \rightarrow \infty} \sum_{k=1}^n \frac{\ln s_i^k}{t_0}, \quad (36)$$

converge. Here λ_1 is the largest Lyapunov exponent and λ_2 is the second largest one. By adding more and more trajectories, in principle, this method can be used to obtain the whole Lyapunov spectrum with arbitrary accuracy. The time needed to obtain a given Lyapunov exponent depends on how fast the procedure converges.

At first glance, the applicability of this method to lattice gauge theory is questionable. The reason is that while the meaning of rescaling and orthogonalization is quite obvious in a Euclidean phase space, it is less clear in the case of a gauge field, where the phase space is curved as well as constrained by Gauss' law. The problem of curvature is relatively simple. One possible approach is to transform the link variable $U_{x,i}$ back to the vector potential A_i^a , and to work in the phase space formed by electric fields and vector potentials, for which the geometry is Euclidean. In the case of SU(2), we have yet a simpler method. Each SU(2) group element is represented by a normalized quaternion. When performing orthogonalization and rescaling, we can simply treat all components of the quaternion as independent cartesian coordinates, because locally the metric of the curved space is Euclidean.

Surprisingly, Gauss' law also does not pose a serious threat, for the following reason. When we rescale the separation vectors d_i , we indeed violate Gauss' law. But if the distance D_i is small, then the violation of Gauss' law is of second order in D_i . If we limit ourselves to sufficiently small $D_i(t_0)$, then the violation of Gauss' law in each rescaling step is negligible. We next observe that the evolution of the system respects Gauss' law, so the violation does not increase with time. On the other hand, the next rescaling decreases the previous violation of Gauss' law by a (large) scale factor, so the violations do not accumulate. The same argument applies to the small changes in the choice of gauge induced by the linear rescaling procedure.

We have used this method to study the SU(2) theory and have measured the largest two Lyapunov exponents. We indeed find that the violation of Gauss' law remains of the order of 10^{-6} . The result of a typical run for the Lyapunov exponents is shown in Figure 8 for a configuration with scaled energy $g^2 E a = 4.06$. The solid line corresponds to the largest exponent and the dotted line to the second largest one. They converge at $t \approx 100$. Note the time scale of saturation of the distance $D(t)$ in the case without rescaling is about 30 at the same energy. The result obtained with our new, improved method, $\lambda_0 = 0.667$, is very close to, but slightly lower than, our previous result $4.06/6 = 0.677$, where we did not use the rescaling technique. We note that the results for the Lyapunov exponents generally converge from above, i.e. the Lyapunov exponents are overestimated when the trajectories are not followed for sufficiently long time. We also observe that λ_1 is almost identical to λ_0 . The reason is that, as we are going to show next, there exists a whole Lyapunov spectrum which forms a continuous curve in the thermodynamic limit.

G. Lyapunov Spectrum

The above method, in principle as well as in practice, can be extended to obtain the whole Lyapunov spectrum for small lattices. For each additional Lyapunov exponent, we need to integrate one more trajectory so as to form one additional linearly independent vector d_i . If we want to calculate ν_L Lyapunov exponents, we need to run $\nu_L + 1$ configurations simultaneously, from which we can form ν_L separation vectors and calculate the ν_L largest Lyapunov exponents. Practically, the computational resources put limits on the possible size of the lattice for which we can obtain the whole Lyapunov spectrum. We have performed studies with 1^3 , 2^3 and 3^3 lattices. Fortunately, we found that the spectrum starts to scale as early as size 3^3 , which permits us to extrapolate the result to the thermodynamic limit.

We have calculated the complete spectrum for 1^3 and 2^3 lattices. The results for the latter are shown in Figure 9. On a N^3 lattice the dimension of phase space is $9N^3 \times 2$, because there are three vector and three color directions at each site for magnetic and electric fields. This amounts to a total number of 144 Lyapunov exponents for $N = 2$. We can see that the spectrum is divided into three equal parts. The first one third of Lyapunov exponents are positive, while the second one third are all zero, and the last one third of exponents are the negative of the first one third. The vanishing Lyapunov exponents account just for all the degrees of freedom associated with static gauge transformations and with conservation of Gauss' law, each equal in number to three times the number of lattice sites. Thus our results confirm the general properties of Lyapunov spectra[34]. The results for a 1^3 lattice are basically the same, but the Lyapunov spectrum consists only of 18 numbers. The value of the largest Lyapunov exponent is consistent with the result obtained earlier for the model of spatially constant Yang-Mills potentials (see section 2.4).

In Figure 10 we show the scaling of the Lyapunov spectrum, where we compare the results from a 2^3 lattice and a 3^3 lattice. To save computation time, we have calculated only the positive Lyapunov exponents for the 3^3 lattice. In both cases, the initial configurations are chosen similarly. For presentation the Lyapunov exponents were scaled with respect to the largest exponent λ_0 in each case. The indices labeling the Lyapunov exponents are scaled to the total number of Lyapunov exponents, i.e. 144 for a 2^3 lattice and 486 for a 3^3 lattice. The two lines coincide nicely, exhibiting an early scaling behavior.

The scaled Kolmogorov-Sinai entropy, i.e. the sum over all positive Lyapunov exponents, is:

$$\frac{\sum_i \lambda_i}{N^3 \lambda_0} \approx 2, \tag{37}$$

where N^3 is the size of the lattice. We point out that at this small lattice size, the spectrum does not yet scale with energy. But we know from section 3.4 that this scaling appears at

a lattice of size 6^3 , where we found $\lambda_0/g^2E \approx \frac{1}{6}$. If we combine both scaling laws, we can estimate the Lyapunov spectrum in the thermodynamic limit, from which we obtain the Kolmogorov-Sinai entropy density

$$\dot{\sigma}_{\text{KS}} = \frac{1}{(Na)^3} \sum_i \lambda_i \approx \frac{1}{9} g^2 \varepsilon, \quad (38)$$

where $\varepsilon = 3E/a^3$ denotes the energy density, and E is the average energy per elementary plaquette. Making use of the thermodynamic relation $\sigma T = \varepsilon + P = \frac{4}{3}\varepsilon$, we find that the characteristic entropy growth rate for SU(2) is given by

$$\frac{\dot{\sigma}_{\text{KS}}}{\sigma} \approx \frac{1}{9} g^2 \frac{\varepsilon}{\sigma} = \frac{1}{12} g^2 T. \quad (39)$$

The above method is quite successful for SU(2) gauge theory, but it is not obvious how to apply it to SU(3) gauge fields. The reason is that this method relies on the quaternion representation, which is quite special for the group SU(2). We have also developed a more general method to obtain the Lyapunov spectrum, which can be used to study SU(3) gauge theory. Again the basic idea is simple. We want to directly consider the motion of vectors in the tangent space built upon the phase space $\{E_{x,i}, U_{x,i}\}$. The tangent space of $E_{x,i}$ is simple, the vectors just being given by $\delta E_{x,i}$. We must be more careful specifying a vector in the tangent space to $U_{x,i}$. Here, to be consistent with our definition of the conjugate momenta $E_{x,i}$ as the left group generators, we define a vector $b_{x,i}$ in the tangent space of $U_{x,i}$ as $\delta U_{x,i} = i b_{x,i} U_{x,i}$. A vector in the complete tangent space is the direct product of $b_{x,i}$ and $\delta E_{x,i}$. The linear evolution equations for $b_{x,i}$ and $\delta E_{x,i}$ can be derived and integrated along with the equations of motion in phase space. Initially choosing ν_L vectors, we can again obtain ν_L Lyapunov exponents. The results for SU(2) by this method is shown in Figure 11, in comparison with the result obtained by the previous method. We observe good agreement for large positive Lyapunov exponents, but increasing deviations for the smaller ones. These deviations can be eliminated by demanding higher numerical precision for the second method.

IV. OTHER LATTICE FIELD THEORIES

In this section, we want to apply our method to several other interacting fields. We calculate their largest Lyapunov exponents and investigate how they scale with energy, in order to determine the nature of the stochastic behavior of the various field theories.

A. U(1) Gauge Theory

How characteristic is the observed behavior for the SU(2) gauge theory? Of course, one would expect a similar chaotic behavior for higher SU(N) gauge theories, because SU(2) is a subgroup of SU(N). However, one may expect a completely different behavior in the case of compact U(1), which has no self-interaction of gauge bosons in the continuum limit. The gauge group U(1) is easily obtained as a one-parameter abelian subgroup of SU(2). Not unexpectedly, we find quite different results in this case. For small values of the parameter $g^2 Ea$ there is no discernable exponential divergence of adjacent field configurations. As shown in Figure 12, $\lambda_0 a$ suddenly begins to grow rapidly for values $g^2 Ea \approx 2$. However, the dependence is highly nonlinear, reminiscent of the behavior of many nonlinear dynamical systems. This proves that the approximately linear relationship between $\lambda_0 a$ and $g^2 Ea$ found for the gauge group SU(2) is far from trivial. The latter is obviously associated with the nonabelian nature of this group. It is also worthwhile noting that $\lambda_0 \rightarrow 0$ for $a \rightarrow 0$ in U(1), i.e. the maximal Lyapunov exponent λ_0 for the compact U(1) lattice gauge theory vanishes in the continuum limit.

B. SU(3) Gauge Theory

Since SU(3) contains SU(2) as a subgroup, we will certainly expect that SU(3) gauge theory is chaotic. This expectation is borne out by our study of the dynamics of SU(3) gauge fields on a lattice, which shows the same type of exponential instability [30]. While the basic procedure here is same as in SU(2), technically SU(3) is more complicated than SU(2). But nevertheless, since SU(3) is physically relevant as the gauge theory of the strong interaction, it is worthwhile to study its general dynamical properties.

Whereas a SU(2) group element can be represented by a quaternion with only one redundant variable, there is no such simple representation for a general SU(3) group element. In principle we can use the exponential representation with 8 angles as independent variables. But as in the case of SU(2) this would involve many time consuming trigonometric manipulations required to carry out a group multiplication. In our simulations we have, therefore, directly used the matrix representation, i.e. we represent every group element by a unitary 3×3 matrix. With the cost of 10 redundant variables for each link the group multiplication is directly realized by matrix multiplication which only involves multiplications and additions.

Another difference we shall point out is that it was necessary to be more careful in choosing the initial states here than in the case of SU(2), because the topological structure of the group space of SU(3) is more complicated. SU(3) is an eight-parameter Lie group and not all directions in group space are equivalent. Simply choosing angles at random in a

certain representation of the group parameters [31] can lead to a sampling of gauge fields that differs strongly from the thermal ensemble. It therefore proved necessary to choose the initial state by the heat-bath method [27, 32], which is straightforward but numerically expensive especially at low temperatures where the rejection rate is large. All other considerations, especially the scaling property (21), carry over to SU(3).

Our numerical results, obtained by evolving the thermalized initial condition, are presented in Figure 13. They show again a close to linear dependence between λ_0 and $g^2 E$, but with a different slope than for SU(2). To good approximation we find:

$$\lambda_0 a \approx \frac{1}{10} g^2 E a. \quad (40)$$

We investigated several cases with non-thermalized initial conditions, specified by restricting some angles to a certain limited range. These initial conditions lead to exponential divergence rates lying above the line (40). We surmise that this reflects the lack of complete randomization of the field configuration during the limited time interval until the distance measure saturates. This suggests the importance of the thermalized initial condition, when the rescaling method is not applied. We have also tried a different definition of distance

$$D^E[U, U'] = \frac{1}{N_p} \sum_x \left| \sum_i \text{tr}(\dot{U}_{x,i}^\dagger \dot{U}_{x,i}) - \text{tr}(\dot{U}'_{x,i} \dot{U}'_{x,i}) \right|, \quad (41)$$

corresponding to the sum of the absolute value of local difference in the electric energy. The rise of $\ln D^E(t)$ is coincident with that exhibited by $\ln D(t)$ except for the initial oscillatory region. This is within our expectation because the chaoticity of a system is an intrinsic property and it does not depend on a particular choice of the distance measure.

C. Massless Scalar Field

One question concerning the chaoticity of nonabelian gauge fields is whether the chaoticity is just a consequence of the nonlinearity of the field equations, or whether it is related to the particular form of the nonabelian gauge interaction. In this respect, we study the classical Φ^4 theory described by the Lagrangian

$$L = \partial_\mu \Phi^\dagger \partial^\mu \Phi - \mu^2 \Phi^\dagger \Phi - g^2 (\Phi^\dagger \Phi)^2. \quad (42)$$

The lattice formalism for interacting Higgs and gauge fields was given by Ambjørn et al. [35]. We here study a special case, i.e. the massless limit of an iso-doublet complex scalar field, which has four real field components, without the gauge field. In the massless limit ($\mu = 0$), just like in the case of a gauge theory, the corresponding classical lattice theory is scale invariant, in the sense that the self-coupling g^2 of the scalar field and the lattice

spacing a can be scaled out entirely and the system has no free parameter except the total energy.

Using the same method as before, we measured Lyapunov exponents of the massless scalar field on the lattice. In Figure 14 we show λ_0/g^2E as function of g^2Ea . Observe that the maximal Lyapunov exponent for the scalar field is much smaller than that for gauge fields with the same energy. Second, we find that the ratio λ_0/g^2E tends to zero at small g^2Ea , suggesting a vanishing Lyapunov exponent in the continuum limit $a \rightarrow 0$. This result is consistent with our understanding of the relation between the maximal Lyapunov exponent and the damping rate of the long wavelength modes. The thermal perturbation theory calculation shows, unlike in the case of nonabelian gauge fields, that the damping rate of the long wavelength mode of the scalar field vanishes at the order of g^2 . This result shows that not all nonlinear classical continuum field theories are chaotic.

D. Massive SU(2) Vector Fields

This is the first step toward the understanding of chaoticity in the electroweak interaction, where the gauge symmetry is spontaneously broken by a Higgs field. We want to study how a mass term affects the chaotic behavior, in order to find a hint of how the interaction between the Higgs field and the gauge field may affect the chaoticity of the latter. In Figure 15, we show the largest Lyapunov exponents at various energies for theories with different vector boson mass. The same scaled variables are used as before, but here the mass parameter m cannot be scaled out. It is related to the mass M of the vector field in the continuum theory as $M = m\hbar/2a$. For comparison, the results for the massless gauge theory are shown as solid squares, which are fit by a straight line with a coefficient of $\frac{1}{6}$. The hollow squares are for $m = 0.2$, and the crosses are for $m = 4$. They more or less lie on a straight line. We observe that the effect of a mass term is to reduce the chaoticity of the system, or in other words, the mass term has a stabilizing effect on the trajectories of the field configurations. This effect is consistent with studies of the simple system (12), where the amount of chaoticity depends on the relative strength of the nonlinearity and the harmonic potential [11].

E. Spontaneously Broken SU(2) Yang-Mills Theory

The pure SU(2) and SU(3) Yang-Mills gauge theories are the primary tools for studying nonperturbative QCD related phenomena, such as properties of a hot quark-gluon plasma. The spontaneously broken SU(2) Yang-Mills theory, in which a charged scalar isodoublet field, the Higgs field, is coupled to the gauge boson, is a model of the electroweak gauge

theory. It is used to study the high-temperature limit of the standard model of particle physics, in particular, the phenomenon of baryon number violation at temperatures around the electroweak phase transition temperature of $T = 200$ GeV.

In the limit of vanishing Weinberg angle, the Hamiltonian describing this model is given by

$$H = \int d^3x \left[\frac{1}{2} E_i^a E_i^a + \frac{1}{4} F_{ij}^a F_{ij}^a + \dot{\Phi}^\dagger \dot{\Phi} + (D_i \Phi)^\dagger (D_i \Phi) - \mu^2 \Phi^\dagger \Phi + \lambda (\Phi^\dagger \Phi)^2, \right] \quad (43)$$

where the dot symbol denotes time derivative,

$$\Phi = \begin{pmatrix} \phi_1 + i\phi_2 \\ \phi_3 + i\phi_4 \end{pmatrix} \quad (44)$$

is a charged Higgs doublet in the fundamental representation of SU(2), and the gauge field is described by vector potentials $A_t^a(x)$ in the temporal axial gauge $A_0^a = 0$. In the numerical simulation we again discretize the gauge fields and represent them by link variables $U_{x,i}$, which are identified with real-valued quaternions. The Higgs doublet is also represented as a quaternion. However, its length (determinant) is also a dynamical degree of freedom, which we denote by R :

$$R^2 = \frac{1}{2} \text{tr} (\Phi^\dagger \Phi). \quad (45)$$

Following the notation of Amjorn et al. [35], we introduce a unit length quaternion V for the representation $\Phi = RV$. This factorization is a useful way to separate the gauge-invariant and the gauge-dependent degrees of freedom of the Higgs fields Φ . Nevertheless, in most formulas we shall use the matrices Φ, Φ^\dagger , for brevity.

The lattice regularized version of the Hamiltonian (43) is based on the link-variables $U_{x,i}$, defined as in eq. (16) and the site-variables, Φ_x , or equivalently $R_x V_x$, for the rescaled Higgs field matrix

$$\Phi_x = \frac{a}{\sqrt{\beta_H}} \Phi(x). \quad (46)$$

The Hamiltonian consists of three terms. The first one is the same as for the pure Yang-Mills theory

$$H_W = \frac{\beta_G}{a} \left[\frac{a^2}{4} \sum_{x,i} \text{tr} (\dot{U}_{x,i}^\dagger \dot{U}_{x,i}) + \sum_{x,ij} (1 - \frac{1}{2} \text{tr} U_{x,ij}) \right], \quad (47)$$

where $U_{x,ij}$ again stands for a plaquette quaternion. The second term in the Hamiltonian describes the free Higgs doublet and its coupling to the gauge field

$$H_{HW} = \frac{\beta_H}{a} \left[\sum_x \frac{a^2}{2} \text{tr} \dot{\Phi}_x^\dagger \dot{\Phi}_x + \sum_{x,i} \frac{1}{2} \text{tr} \Phi_x^\dagger (\mathbf{1} - U_{x,i}) \Phi_{x+i} \right] \quad (48)$$

where Higgs fields on neighboring sites x and $x + i$ are coupled by the lattice transport operator $(\mathbf{1} - U_{x,i})$, that generates the gauge covariant derivative in the continuum limit. The last term in the Hamiltonian accounts for the self-interaction of the Higgs fields

$$H_{\text{H}} = \frac{\beta_{\text{R}}}{a} \sum_x (R_x - 1)^2, \quad (49)$$

where R_x is defined by eq. (45). The coupling parameters β_{G} , β_{H} , and β_{R} , introduced into the lattice Hamiltonian are related to the parameters of the original continuum Hamiltonian as follows

$$\mu^2 = \frac{\beta_{\text{R}}}{\beta_{\text{H}}} \frac{1}{a^2}, \quad \lambda = \frac{\beta_{\text{R}}}{\beta_{\text{H}}^2}, \quad g^2 = \frac{4}{\beta_{\text{G}}}. \quad (50)$$

The vacuum expectation value of the Higgs field in the spontaneously broken phase is obtained from the minimum of the energy term H_{H} , and can be scaled to unity. The symmetry breaking, where $\langle R_x \rangle = 1$, occurs when

$$\beta_{\text{H}} > \frac{\hbar}{3} - \frac{\hbar^2}{27\beta_{\text{G}}}. \quad (51)$$

In this phase large Higgs and gauge boson masses are generated:

$$M_{\text{H}}^2 = 4\hbar^2 \lambda \langle \Phi^2 \rangle = \frac{4\beta_{\text{R}}}{\beta_{\text{H}}} \frac{\hbar^2}{a^2} \quad (52)$$

and

$$M_{\text{W}}^2 = \frac{1}{2} \hbar^2 g^2 \langle \Phi^2 \rangle = \frac{2\beta_{\text{H}}}{\beta_{\text{G}}} \frac{\hbar^2}{a^2}. \quad (53)$$

The equations of motion derived from the lattice Hamiltonian

$$H = H_{\text{W}} + H_{\text{HW}} + H_{\text{H}}, \quad (54)$$

are identical to (24, 25) for the time derivatives of the components of the link variables, $u_{x,i}^a$ and $u_{x,i}^0$. The three electric fields $E_{x,i}^c$ on each link are updated according to

$$\dot{E}_{x,i}^a = \frac{i}{ag^2} \sum_j \text{tr} \left[\frac{1}{2} \tau^a (U_{x,ij} - U_{x,ij}^\dagger) \right] + \frac{\beta_{\text{H}}}{\beta_{\text{G}}} \text{tr} \left(\frac{1}{2} \tau^a U_{x,i} \Phi_{x+i} \Phi_x^\dagger \right), \quad (55)$$

where the sum again runs over all four plaquettes attached to the link (x, i) . Gauss' law now has the form

$$D_i^{ab} E_i^b - ig(\Phi^\dagger \tau^a \dot{\Phi} - \dot{\Phi}^\dagger \tau^a \Phi) = 0, \quad (56)$$

and remains conserved under time evolution. Finally, the Higgs fields evolve according to

$$\ddot{\Phi}_x = \sum_i (U_{x,i} \Phi_{x+i} + U_{x,-i} \Phi_{x-i}) - \left[6 + \frac{4\beta_{\text{R}}}{\beta_{\text{H}}} (R_x^2 - 1) \right] \Phi_x, \quad (57)$$

where the summation index i runs over all spatial directions ($i = x, y, z$). By introducing an auxiliary variable $\Psi_x = \dot{\Phi}_x$, we transform the set of second-order differential equations into a larger set of coupled first-order differential equations.

Solving the evolution equations (25,55,57) we can study the dynamics of the coupled Yang-Mills-Higgs system, and see how the fields approach thermal equilibrium. In particular, we can investigate the divergence of trajectories in the configuration space. In addition to the already defined gauge-invariant distance measure (29) for the distance between two Yang-Mills fields which is based on the magnetic energy, we measure the distance of Higgs field configurations by

$$D^H[\Phi, \Phi'] = \frac{1}{N^3} \sum_x |R_x - R'_x|, \quad (58)$$

which is also gauge invariant.

Depending on the relative strength of the gauge coupling g and Higgs self-coupling λ different hierarchies in the thermalization rate can be obtained. Figure 16 shows the time evolution of the gauge field and Higgs-field distances (a) in a cross-coupled, $\lambda \approx g$ and (b) in a self-coupling dominated case, $\lambda \gg g$. The logarithmic growth rate, defined as

$$h = \frac{d}{dt} \ln D(t), \quad (59)$$

again depends on the average energy per plaquette. This dependence, counting only the energy per plaquette contained in the gauge field, is somewhat different in the above two cases, $\lambda \approx g$ and $\lambda \gg g$, as shown in Figure 17. At the upper end of the energy scale, $h(E)$ is about the same for the two cases and also agrees with the value (32) for the pure gauge field, $h(E)$ is much smaller for the strongly coupled case (b) for low energies. We also note that the gauge field becomes chaotic faster than the Higgs field in case (b), while they become chaotic equally fast in case (a).

V. THERMALIZATION OF GAUGE FIELDS

A. Thermalization Time

The universal exponential divergence of neighboring gauge field configurations for the gauge groups SU(2) and SU(3) implies that the entropy S of an ensemble of gauge fields grows linearly with time [33]:

$$S(t) = S_0 + t \sum_{\lambda_i > 0} \lambda_i, \quad (60)$$

until the available microcanonical phase space is filled and the system is equilibrated. In perturbation theory, the average energy E per plaquette is related to the temperature as [35]:

$$E \approx \frac{2}{3}(n^2 - 1)T \quad [\text{for SU}(n)]. \quad (61)$$

It follows that the characteristic entropy growth rate, i.e. the thermalization rate is given by

$$\Gamma_0 \equiv \lambda_0 \approx \begin{cases} 0.34 g^2 T & [\text{SU}(2)] \\ 0.54 g^2 T & [\text{SU}(3)] \end{cases}, \quad (62)$$

where we have inserted our best-fit numerical values from eqs. (32) and (40). Apart from a factor two, these values are remarkably close to those for the thermal damping rate for a gauge boson at rest obtained by Braaten and Pisarski [12]

$$\gamma_0 = 6.635 \frac{N}{24\pi} g^2 T = \begin{cases} 0.175 g^2 T & [\text{SU}(2)], \\ 0.264 g^2 T & [\text{SU}(3)]. \end{cases} \quad (63)$$

At first sight, the relation $\Gamma_0 \approx 2\gamma_0$ is quite surprising because these two quantities appear in totally different contexts and are calculated with different methods. On the one hand, the damping rate is the imaginary part of the self energy of a quasi-particle in a thermal gauge system and is calculated in the framework of effective quantum field theory. On the other hand, the Lyapunov exponent is a classical dynamical quantity describing the divergence of two classical gauge field trajectories.

Although we do not yet know how to establish a direct relation between these two quantities, we understand that this similarity does not arise without reason. The two quantities, though very different from their contexts, both describe how fast a non-equilibrated gluon system approaches thermal equilibrium. The relevance of λ_0 is clear from the above discussion. The connection of $\gamma(\omega)$ is apparent from the relation [36]

$$f(\omega, t) = \frac{1}{e^{\omega/T} - 1} + c(\omega)e^{-2\gamma(\omega)t}, \quad (64)$$

where $f(\omega, t)$ is time-dependent gauge boson distribution function, and the first term on the right-hand side is the Bose distribution. Obviously, 2γ describes the rate of approach to equilibrium. It is possible to show that the gluon damping rate is basically a quantity of semi-classical origin [30].

Finally, let us estimate the gluon thermalization quantitatively. Figure 18 shows $\tau_S = \Gamma_0^{-1}$ as function of temperature. For the gauge coupling constant g^2 we have used the renormalized running coupling constant of SU(3) gauge theory, which in the one-loop approximation is given by:

$$g^2(T) = \frac{16\pi^2}{11 \ln(\pi T/\Lambda)^2}, \quad (65)$$

where $\Lambda \approx 200$ MeV is the QCD scale parameter. For temperatures in the range $T = 300 - 500$ MeV, which are realistically accessible in relativistic heavy-ion collisions, the thermalization time is less than 0.4 fm/ c , or about 10^{-24} s. This promises the rapid formation of a locally thermalized gluon plasma in these collisions at sufficiently high energy.

B. Self-Thermalization of Gauge Fields

With the numerical tools in this context we can study the thermalization of gauge fields by direct simulation of their real-time evolution. Here we show that a nonabelian gauge field far off equilibrium approaches a thermally equilibrated state very rapidly. A thermally equilibrated state is the state in which the energy distribution over the microscopic degrees of freedom does not change with time and takes the thermal equilibrium form, which can be calculated from the canonical Gibbs ensemble. In order to study the process of thermalization, we must decide on which particular energy distribution we want to monitor. Here we choose as our monitor $P(E_M)$, the distribution of magnetic energy on the elementary plaquettes over the whole lattice. The reason we prefer magnetic energy to electric energy is that the thermal distribution of the former can also be obtained using a heat bath algorithm, and so we can compare the results from time evolution and those from a heat bath method. $P(E_M)$ is obtained by counting the number of plaquettes that have magnetic energy between $E_M - \Delta E_M/2$ and $E_M + \Delta E_M/2$. ΔE_M should be sufficiently small so that $P(E_M)$ is smooth but large enough to provide good counting statistics. Starting from an arbitrary initial state, we can measure the time evolution of $P(E_M)$. If we find that it reaches some stable form we conclude that the system is thermally equilibrated.

We numerically integrate the equations of motion for given initial conditions and measure the energy distribution functions $P(E_M, t)$. The behavior in SU(2) and in SU(3) is rather similar. Here we concentrate on the SU(3) results. In Figure 19 we show the time evolution of $P(E_M)$ for SU(3). The corresponding initial averaged energy per plaquette is $E = \langle E_M \rangle = 1.73$. The plot shows $\ln(P(E_M, t)/E_M^3)$ for reasons that will become clear below. The solid line denotes the initial distribution at $t = 0$. The dotted and short-dashed lines are for $t = 0.5$ and $t = 1.5$ respectively. The long-dashed line shows the final distribution reached at $t = 3$, whereafter no noticeable change is observed. The thermalization time is compatible with the inverse of the maximal Lyapunov exponent, which is $\lambda_0^{-1} = 10(g^2 E)^{-1} = 7.7$ for SU(3). The final magnetic energy per plaquette is 0.84 which is almost half of the total energy. This is not always true on the lattice where the magnetic energy is limited from above because of the compact nature of the gauge group manifold. But in our example the total energy is small and the compactness is not a relevant influence.

We have obtained equilibrated distributions $P(E_M)$ for different initial energies in both

SU(2) and SU(3). These distributions can all be almost perfectly fit by

$$P(E_M) = \mathcal{N} f(E_M) \exp(-E_M/T_s), \quad (66)$$

where \mathcal{N} is a normalization constant, and T_s is a “temperature” parameter. $f(E)$ is the single plaquette phase space factor defined as

$$f(E_M)dE_M = \int \delta(E_M - E[U])dE_M d\mu(U), \quad (67)$$

where $E[U] = 2\text{Re}(n - \text{tr } U)$ is the magnetic energy of a single free plaquette for SU(n) and $d\mu(U)$ is the Haar measure. Although the distribution looks like a Boltzmann distribution and T_s like a temperature, we have shown that the real temperature of the system differs from T_s . Their relation is shown in Figure 20 for SU(2). While the ratio $T_s/T \rightarrow 1$ at high temperature, it decreases with T when $T < 2$ and finally it reaches $\frac{2}{3}$ in the limit $T = 0$. We expect a similar behaviour for SU(3). This implies that in the low temperature limit the number of effective degrees of freedom is $2/3$ of that in the high temperature limit.

VI. CONCLUSION AND FUTURE DEVELOPMENTS

The studies of lattice gauge fields reviewed here have considerably extended our knowledge of the properties of the dynamics of classical nonabelian gauge fields. This work began with the results of Matinyan, Savvidy and others more than a decade ago. We now know that the classical Yang-Mills fields are strongly chaotic at all energies. We have obtained the complete Lyapunov spectrum and shown that it scales even for very small lattice sizes. We are thus close to a full understanding of the classical Yang-Mills equations from the point of view of classical dynamics. We have also learned that, although other field theories show signs of chaotic behavior on the lattice, as well, their scaling properties imply that the chaoticity disappears in the continuum limit. This suggests that the chaotic behavior of nonabelian gauge theories is a nontrivial property of these theories.

What are the consequences of the chaotic nature of the classical Yang-Mills theory? We have already studied its application to thermalization at finite temperature. Another possible application is the old idea [37] that the chaoticity may be related to the problem of color confinement. In order to investigate this conjecture, as well as other implications, more thoroughly, the following two possible directions of future research are important.

In order to connect the results of classical gauge field dynamics to the underlying quantum field theory, we must understand the corrections from quantum effects. This means that we must develop appropriate semi-classical methods that link the classical limit to quantum physics. We have recently begun to explore a variational method using Gaussian wave packets for lattice gauge fields and found indications that the quantum corrections enhance

the chaoticity [38]. However, it is known that when a system is chaotic in the classical limit, the quantum evolution of a initially localized Gaussian wave packet tends to disperse the wave packet rapidly [3]. This is easily understood in the path integral formalulation of the quantum theory. A more realistic approach must account for this property. One possible approach is the Wigner function formulation mentioned in section 2.1. However, Wigner functions for gauge fields involve many subtleties [39], and it is not quite clear how the definition of a Wigner function should be best applied to gauge fields on a lattice.

Secondly, the studies have so far been restricted to gauge fields and scalar fields. Since, in reality, the gauge fields are always coupled to fermion fields, a natural question is what role the fermions play in this context. Fermions cannot be treated classically. As a possible solution, one could consider a hybrid model describing the interaction of the quantum evolution of matter fields with the classical evolution of the gauge fields. This requires the solution of the time-dependent Dirac equation on the lattice, which is equivalent to a quantum cellular automaton [40].

We must bear in mind that numerical studies of the real-time evolution of (quantum) field theories on lattices are in their infancy. The results obtained so far indicate that interesting results can be obtained from such investigations, and there is reason to hope that further progress is possible.

Acknowledgment: This work has been supported in part by the U. S. Department of Energy (Grant DE-FG05-90ER40592) and by a computing grant from the North Carolina Supercomputing Center. We thank S. Matinyan for many illuminating discussions. One of us (B.M.) thanks the Institute of Nuclear Theory at the University of Washington for its hospitality and the Department of Energy for partial support during the completion of this work.

-
- [1] *Electronic mail addresses:*
T.S. Biró: ug12@ddagsi3.gsi.de, C. Gong: gong@phy.duke.edu,
B. Müller: muller@phy.duke.edu, A. Trayanov: nasco@phy.duke.edu.
- [2] see e.g.: J. Ford and G. Mantico, Amer. J. Phys. **60**, 1086 (1992).
- [3] J. Ford, G. Mantico, and G.H. Ristow, Physica **D50**, 493 (1991).
- [4] E. Wigner, Phys. Rev. **40**, 749(1932) .
- [5] S. John and E. A. Remler, Ann. Phys. **180**, 152 (1987), and refernces therein.
- [6] H.T. Elze and U. Heinz, Phys. Rep. **183**, 81 (1989).
- [7] K. Wilson, Phys. Rev. **D10**, 2445 (1974).
- [8] R.E. Peierls and J. Yoccoz, Proc. Phys. Soc. (London) **A70**, 381 (1957).
- [9] G. 't Hooft, Nucl. Phys. **B79**, 276 (1974); A.M. Polyakov, JETP Lett. **20**, 194 (1974).
- [10] A.A. Belavin, A.M. Polyakov, A.S. Schwartz, and Yu.S. Tyupkin, Phys. Lett. **59B**, 85 (1975).
- [11] S. G. Matinyan, G. K. Savvidy and N. G. Ter-Arutyunyan-Savvidy, Sov. Phys. JETP **53**, 421 (1981); JETP Lett. **34**, 590 (1981).
- [12] E. Braaten and R. D. Pisarski, Phys. Rev. **D42**, 2156 (1990).
- [13] A. Billoire, G. Lazarides, and Q. Shafi, Phys. Lett. **103B**, 450 (1981); T.A. DeGrand and D. Toussaint, Phys. Rev. **D25**, 526 (1981).
- [14] T.S. Biró and B. Müller, Nucl. Phys. **A** (in print).
- [15] B. V. Chirikov and D. L. Shepelyanskii, JETP Lett. **34**, 163 (1981); Sov. J. Nucl. Phys. **36**, 908 (1982).
- [16] E. S. Nikolaevskii and L. N. Shchur, JETP Lett. **36**, 218 (1982); Sov. Phys. JETP **58**, 1 (1983).
- [17] J. Frøyland, Phys. Rev. **D27**, 943 (1983).
- [18] G. K. Savvidy, Phys. Lett. **130 B**, 303 (1983).
- [19] M. Lüscher, Nucl. Phys. **B19**, 233 (1983).
- [20] W. M. Steeb, J. A. Louw, P. G. L. Leach, and F. M. Mahomed, Phys. Rev. **A33**, 2131 (1986).
- [21] P. Dahlqvist and G. Russberg, Phys. Rev. Lett. **65**, 2837 (1990).
- [22] S. G. Matinyan, E. B. Prokhorenko and G. K. Savvidy, Nucl. Phys. **B298**, 414 (1988).
- [23] T. Kawabe and S. Ohta, Phys. Rev. **D41**, 1983 (1990).

- [24] M. P. Joy and M. Sabir, J. Phys. **A22**, 5153 (1989).
- [25] M. Wellner, Phys. Rev. Lett. **68**, 1811 (1992).
- [26] B. Müller and A. Trayanov, Phys. Rev. Lett. **68**, 3387 (1992).
- [27] M. Creutz, *Quarks, Gluons, and Lattices* (Cambridge Univ. Press, Cambridge, 1983).
- [28] J. Kogut and L. Susskind, Phys. Rev. **D11**, 395 (1975).
- [29] S. A. Chin, O. S. van Roosmalen, E. A. Umland, and S. E. Koonin, Phys. Rev. **D31**, 3201 (1985).
- [30] C. Gong, Phys. Lett. **B 298**, 257 (1993) .
- [31] J. P. Bronzan, Phys. Rev. **D38**, 1994 (1988).
- [32] E. Pietarinen, Nucl. Phys. **B190**, 349 (1981).
- [33] See e.g.: A. J. Lichtenberg and M. A. Lieberman, *Regular and Stochastic Motion* (Springer-Verlag, New York, 1983).
- [34] see for example, G. Benettin, C. Froeschle, and J. P. Scheidecker, Phys. Rev. **A19**, 2454 (1979).
- [35] J. Ambjørn, T. Aksgaard, H. Porter, and M. E. Shaposhnikov, Nucl. Phys. **B353**, 346 (1992).
- [36] A. Weldon, Phys. Rev. **D28**, 2007 (1982). Nucl. Phys. **A522**, 591 (1991).
- [37] P. Olesen, Nucl. Phys. **B200**, 381 (1982).
- [38] C. Gong, B. Müller, and T. Biró, Duke University preprint DUKE-TH-93-49.
- [39] H.T. Elze, M. Gyulassy, and D. Vasak, Phys. Lett. **B177** 402 (1986).
- [40] I. Bialynicki-Birula, Univ. Warsaw preprint, (Bulletin Board: hep-th@xxx.lanl.gov - 9304070).

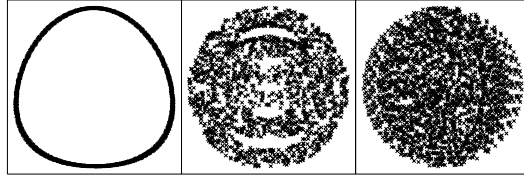


FIG. 1: Poincaré surfaces of section of a single trajectory in the two-dimensional Yang-Mills model ($z(t) \equiv 0$) for three values of the scaling parameter: $r = 4.878$ (left), $r = 0.2$ (center), and $r = 0.0012$ (right).

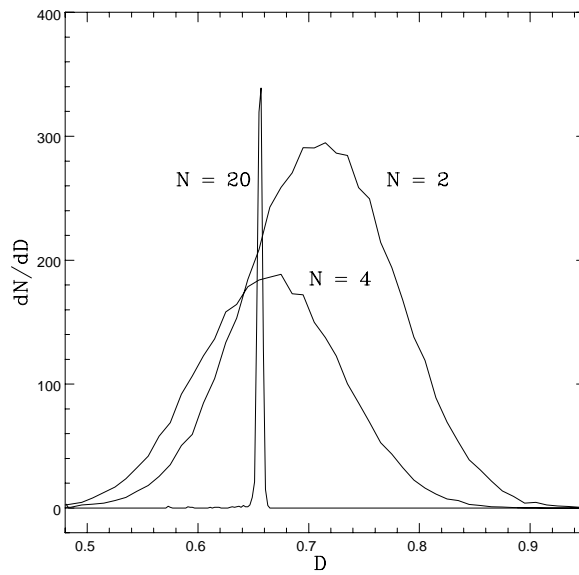


FIG. 2: Distance distribution of points with the same distance D from a given $SU(2)$ field configuration for lattices of size 2^3 , 4^3 , and 20^3 .

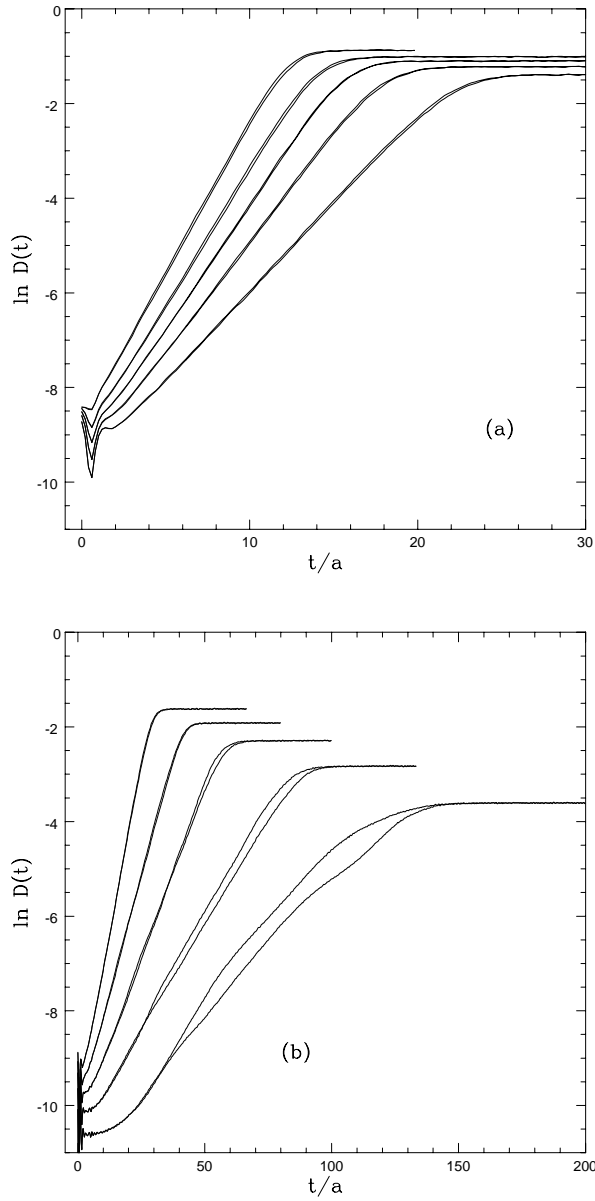


FIG. 3: Evolution of the distance $D(t)$ between neighboring random gauge field configurations for several average energies on a 20^3 lattice. The curves correspond, from top to bottom, to the parameters (a) $\delta = 1, 0.5, 0.45, 0.4, 0.35$; (b) $\delta = 0.3, 0.25, 0.2, 0.15, 0.1$. For every value of δ two curves are shown, which are indistinguishable when $\delta > 0.2$.

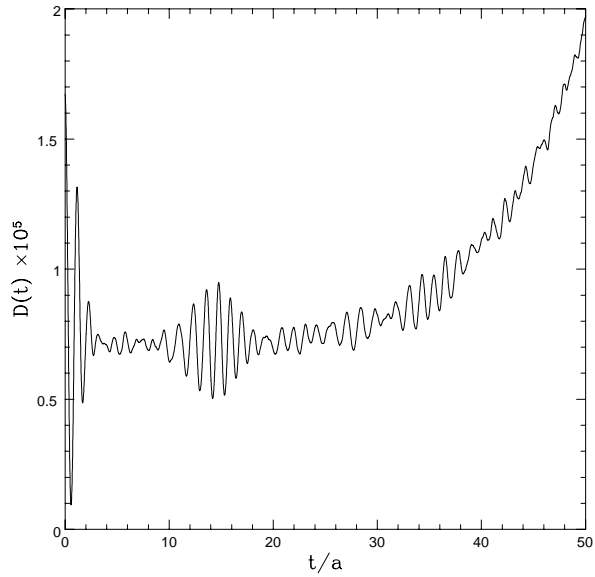


FIG. 4: Initial oscillations in the distance between neighboring field configurations, before the exponential divergence sets in (for $\delta = 0.03$ and $N = 10$).

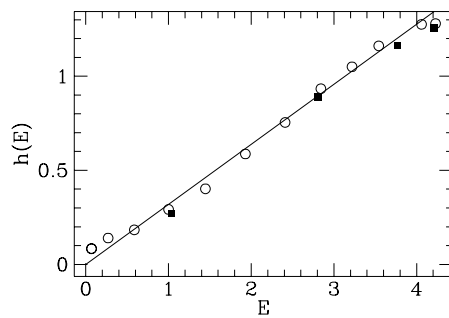


FIG. 5: Dependence of the exponential growth rate h on the average energy per plaquette E of the randomly chosen field configuration, for $a = 0.5$ and $4/g^4 = 1.1185$, and for lattice sizes $N = 20$ (open circles) and $N = 6$ (solid squares). The straight line through the origin is a least-squares fit.

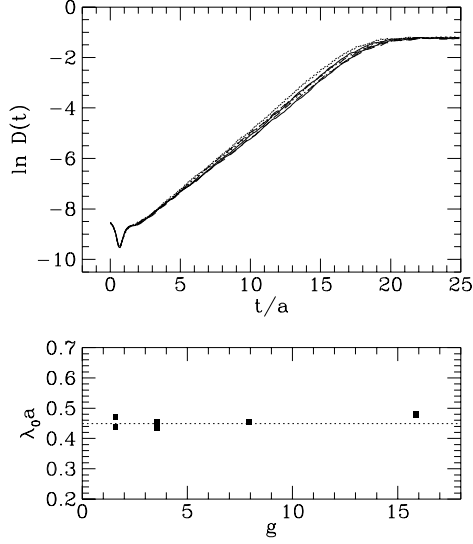


FIG. 6: Scaling of the maximal Lyapunov exponent λ_0 with the variable $g^2 Ea$. At fixed value of the scaling variable, the exponent is independent of the value of g^2 over a wide range. The top part shows $D(t)$ for different choices of g^2 , the bottom part shows the Lyapunov exponent.

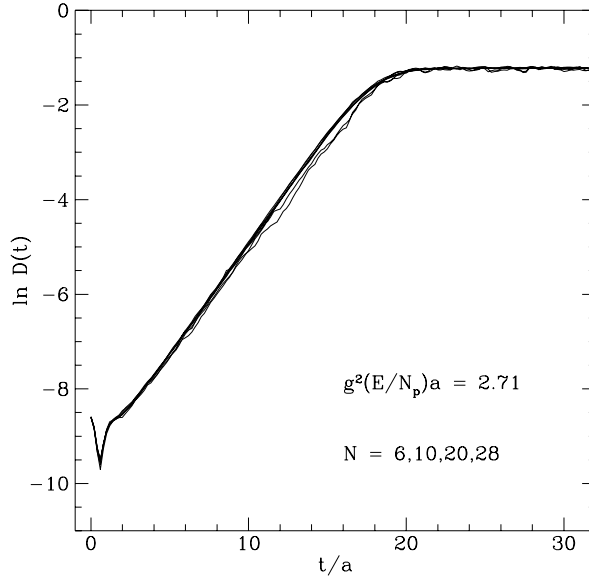


FIG. 7: Dependence of the evolution of the distance between field configurations on the lattice size N . The curves for $N = 6, 10, 20,$ and 28 nearly coincide. All curves correspond to $\delta = 0.4$.

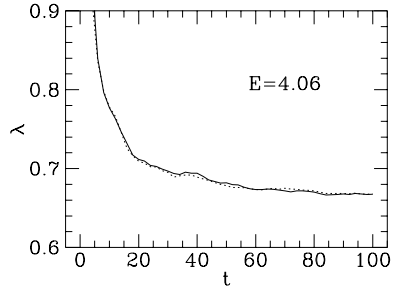


FIG. 8: The two largest Lyapunov exponents for SU(2) determined by the rescaling method. The average of the logarithmic scaling factors s_i^k approaches the limit from above.

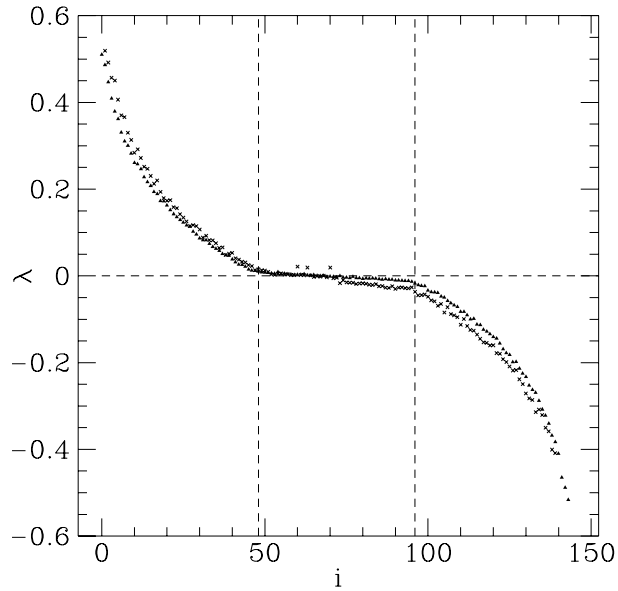


FIG. 9: Complete spectrum of 144 Lyapunov exponents for SU(2) gauge theory on a 2^3 lattice. The trajectories were followed up to time $t/a = 200$ (crosses) and $t/a = 1000$ (triangles). The central third fraction of Lyapunov exponents (enclosed between the vertical dashed lines) corresponds to the unphysical degrees of freedom that describe gauge transformations and deviations from Gauss' law. These exponents converge to zero in the limit $t \rightarrow \infty$.

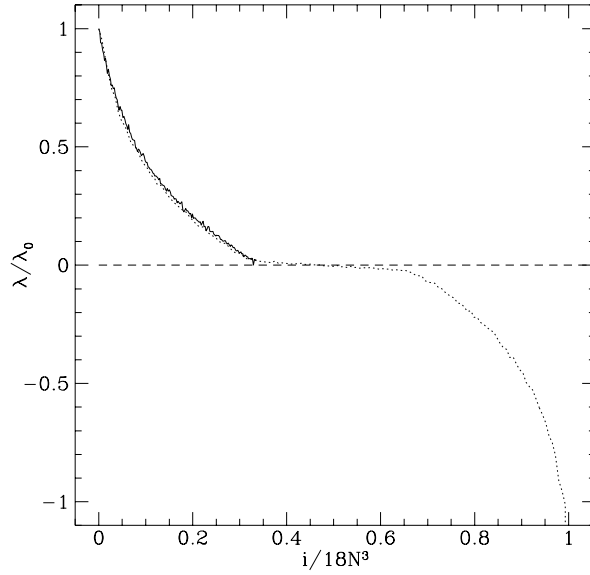


FIG. 10: Scaling of the Lyapunov spectrum with lattice size N . The solid line corresponds to a 3^3 lattice; the dashed line is for a 2^3 lattice. Only the positive Lyapunov exponents are shown. The exponents λ_i are scaled with the maximal Lyapunov exponent for each lattice size, and the index i is scaled with N^3 .

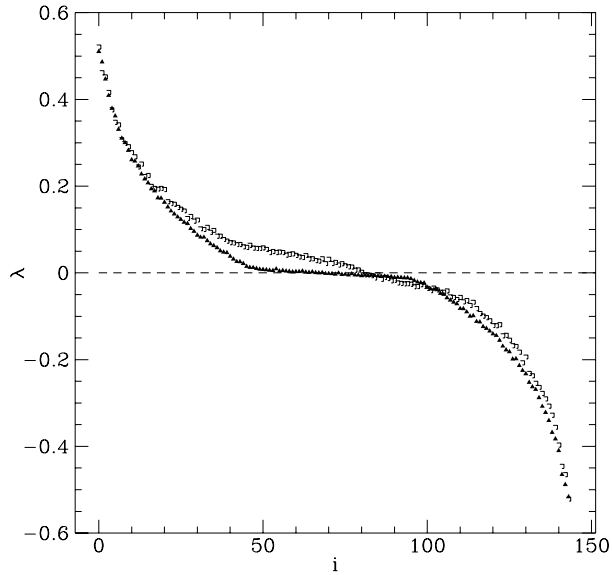


FIG. 11: Lyapunov spectrum for a 2^3 lattice obtained with the second scaling method working directly in the tangent space (hollow square), in comparison with the results based on the first method (solid triangle).

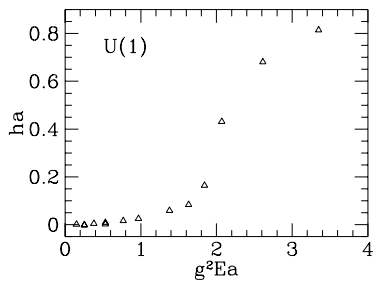


FIG. 12: Dependence of the scaled growth rate ha on the scaling parameter g^2Ea for the gauge group U(1) on a 10^3 lattice. Note the highly nonlinear behavior and the rapid vanishing of ha in the limit $g^2Ea \rightarrow 0$.

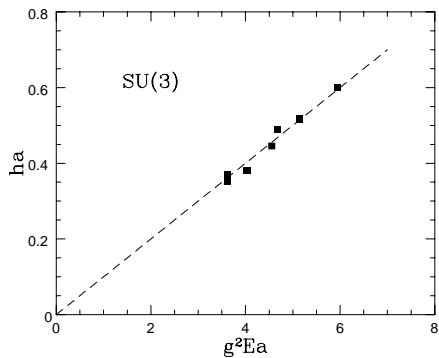


FIG. 13: Dependence of the scaled exponential growth rate $ha = \lambda_0 a$ on the scaling parameter g^2Ea for the gauge group SU(3). The calculations were performed on a 10^3 lattice. The dashed line depicts the fit by eq. (39).

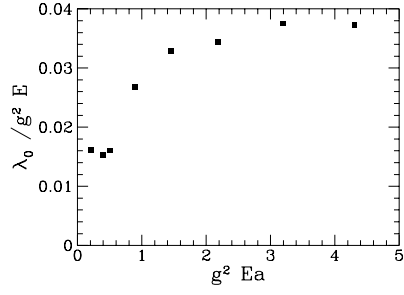


FIG. 14: Maximal Lyapunov exponent for the massless Φ^4 theory as function of the scaling variable $g^2 E a$.

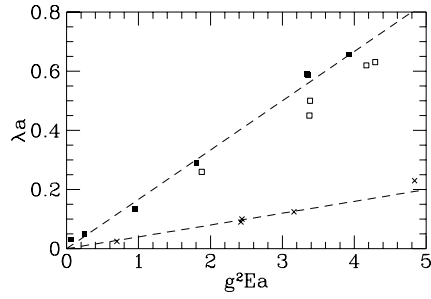


FIG. 15: Maximal Lyapunov exponent for the massive vector field theory as function of the scaling variable $g^2 E a$ for two different values of the vector boson mass: $m = 0.2$ (hollow squares), $m = 4$ (crosses), and for comparison for $m = 0$ (solid squares).

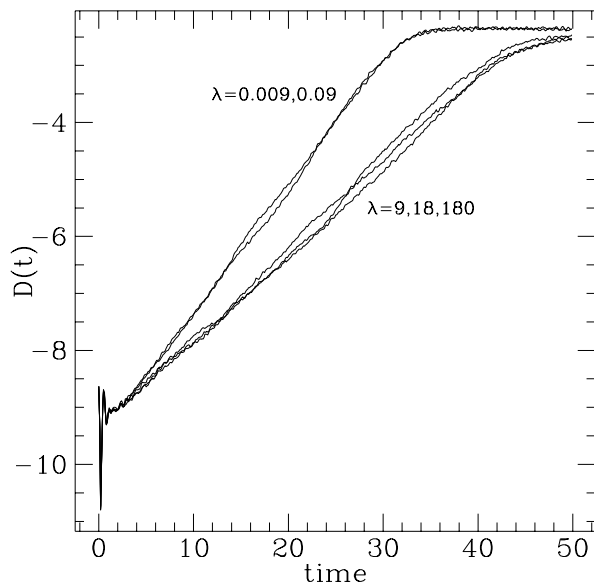


FIG. 16: Time evolution of the gauge field distance and the Higgs field distance for the spontaneously broken SU(2) gauge theory. Part (a) shows a case where the gauge coupling g and the Higgs self-coupling λ are about equal; part (b) corresponds to the case $\lambda \gg g$. For the strongly coupled Higgs field (case b) most of the chaoticity resides in the gauge field.

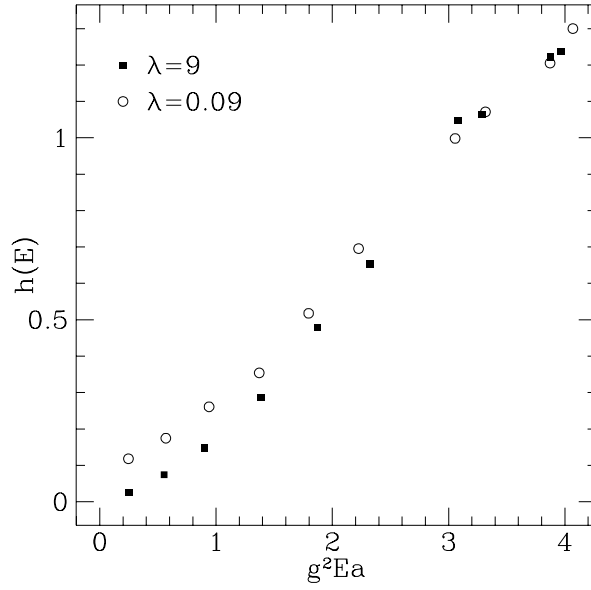


FIG. 17: Maximal Lyapunov exponent of the Yang-Mills Higgs field as function of the variable $g^2 E a$ for the two cases discussed in the caption of Figure 16: (a) $\lambda = 0.9$, (b) $\lambda = 9$. The gauge coupling was $g = 1.375$, and the lattice spacing $a = 0.5$. The weakly coupled Higgs field follows very closely the results obtained for the pure gauge field.

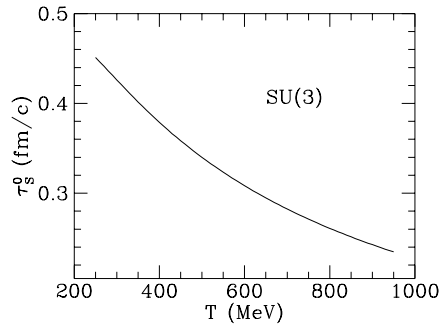


FIG. 18: “Thermalization time” $\tau_S^0 = \lambda_0^{-1}$ for SU(3) as function of temperature T . The scale parameter was taken as $\Lambda = 200$ MeV.

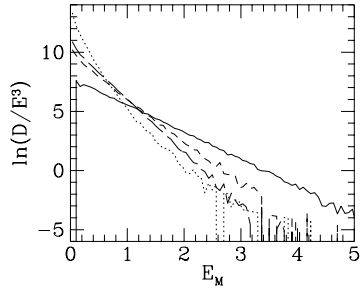


FIG. 19: Time evolution of the distribution of magnetic plaquette energies E_M for a SU(3) gauge field configuration. The plot shows the quantity $P(E_M)/E_M^3$ on a logarithmic scale. The change in slope from the initial distribution (solid line) to the final distribution (long-dashed line) corresponds to the thermalization of all electric field modes, which has a cooling effect on the initially populated magnetic modes.

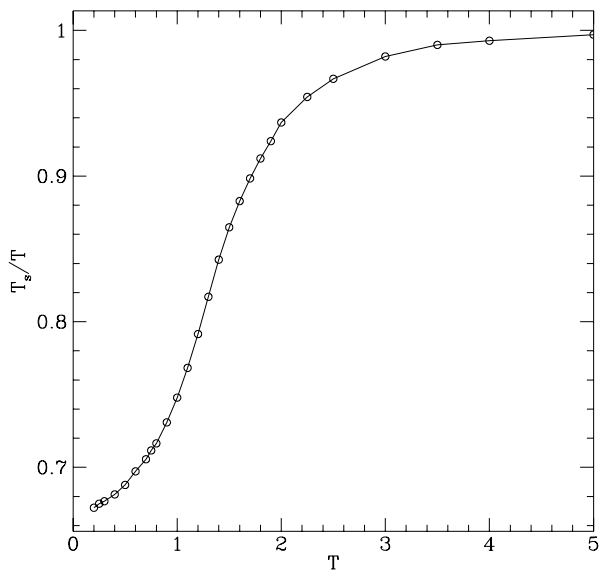


FIG. 20: Slope parameter (“apparent temperature”) T_s of the magnetic energy distribution $P(E_M)$ for the SU(2) gauge field as function of real temperature T . The plot shows the ratio T_s/T , which rises from $\frac{2}{3}$ to 1, because of contributions from the longitudinal plasma modes at higher temperature.